>JSTARS-2025-00845 <

The spatial variation of lake surface water temperature of Poyang Lake in summer and its impact on regional precipitation

Miaoxia Tian, Haibo Zou, Jing Zheng, Anning Huang, Qi Huang

***Abstract*—With Moderate Resolution Imaging Spectroradiometer (MODIS) land surface temperature products, the spatial distribution of lake surface water temperature (LSWT) in Poyang Lake (PL) during summer are explored. Results show that the high-LSWT areas at noon (13:30 local solar time) are mainly located in the southwest, south and east of PL where the water depth is relatively shallow, while the low-LSWT regions are situated in the middle and north of PL where the water depth is relatively deep, and the spatial difference can reach 1.5 °C. This distribution is obviously different from the previous finding (i.e., high LSWT in middle of north of PL, and low LSWT in southwest of PL). By night (01:30 local solar time), the distribution is roughly consistent with that at noon, rather than opposite. This is mainly induced by the relatively high air temperature over the PL region at night, which can not only increase the downward longwave radiation of atmosphere, but also decrease the heat transport from lake to air, favorably reducing the heat loss in PL and slowing down the cooling of PL. To reveal the effects of the spatial variations of LSWT on regional precipitation, two sets of experiments, i.e., non-update (NOUP) experiment with default LSWT and update (UP) experiment with LSWT originated from MODIS data, are conducted, and results show that UP experiment obviously improves precipitation simulation in PL region. Diagnoses indicate that the effects of LSWT on local precipitation are accomplished through adjusting the low-level upward motion and atmospheric instability.**

***Index Terms*—Poyang Lake, Lake surface water temperature, Spatial variation, Precipitation, Atmospheric instability.**

Manuscript submitted at March 8, 2025. This work was supported in part by the National Natural Science Foundation of China under Grant 42275007 and 42301041, in part by the Joint Research Project for Meteorological Capacity Improvement in China under Grant 23NLTSZ004, and in part by the Natural Science Foundation of Jiangxi Province in China under Grant 20242BAB26050 and 2023KYG01001. (Corresponding author: Haibo Zou.)

Miaoxia Tian is with the Key Laboratory of Poyang Lake Wetland and Watershed Research of Ministry of Education & the Key Laboratory of Natural Disaster Monitoring, Early Warning and Assessment of Jiangxi Province, Jiangxi Normal University, Nanchang, 330022, China (e-mail: 18169084380@163.com).

Haibo Zou is with the Key Laboratory of Poyang Lake Wetland and Watershed Research of Ministry of Education & School of Geography and Environmental Science, Jiangxi Normal University, Nanchang 330022, China (e-mail: zouhb@jxnu.edu.cn).

Jing Zheng is with the Meteorological Observatory of Jiangxi province, Nanchang, 330096, China (e-mail: 397561016@qq.com).

Anning Huang is with the School of Atmospheric Sciences, Nanjing University, Nanjing, 210000, China (e-mail: anhuang@nju.edu.cn).

Qi Huang is with the Key Laboratory of Poyang Lake Wetland and Watershed Research of Ministry of Education, Jiangxi Normal University, Nanchang 330022, China (e-mail: huangq@jxnu.edu.cn).

I. INTRODUCTION

LAKE surface water temperature (LSWT) indicates the water temperature at the depth of about 10 cm from the lake surface [1]. It plays a crucial role in biochemical processes and hydrodynamics and can change the level of eutrophication in lakes and their surrounding ecosystems [1-3], ultimately affecting sediment decomposition [4], algal blooms [5], and fish growth [6]. Importantly, LSWT also can change air temperature [7], air moisture [8], and airflow [9-11] over a lake, finally affecting the precipitation in the lake region [12-16].

How does LWST affect local precipitation? In fact, the water and heat exchange between lakes and the overlying air are the ways lakes affect regional weather and climate [8,17]. However, the heat exchange mainly depends on the temperature difference between lakes and the overlying air [18,19]. Although the water vapor exchange directly depends on the saturated vapor pressure deficit (i.e., the difference between saturated vapor pressure and vapor pressure) and wind speed of air over lakes [18-20], the saturated water vapor pressure over lakes is decided by LSWT [21]. Apparently, LSWT affects local precipitation by influencing the exchange of heat and water vapor between lakes and the overlying air. Wright et al. [22] and Zou et al. [23] indicated that the precipitation intensity in a lake region is closely correlated with the LSWT intensity and suggested that the intensity and location of precipitation are closely related to the spatial distribution of LSWT [24].

The variation of LSWT of a lake with space is complex and usually related to the location and depth, as well as the climate background. The LSWTs in the northern part of Erhai Lake, Qinghai Lake, and Dianchi Lake are higher than those in the southern part [25-27], while the LSWT in the northern part of Lake Superior is lower than that in the southern part [28]. The eastern parts of Lake Tahoe, Taihu Lake, Vättern, and Lake Superior are warmer than their western parts [29-31]. Furthermore, the deep-water areas of the Great Lakes in North America [19] and Namco Lake in China [28] are warmer than their shallow-water areas in winter, and in summer the shallow-water areas are in turn warmer than the deep-water areas. Wang et al. [27] also indicated that the central area of Dianchi with deep water was warmer than its near-shore areas with shallow water at nighttime, and in the daytime, the situation was opposite.

Poyang Lake (PL) is the largest freshwater lake and the

second-largest lake in China. It is a seasonal lake, and in summer, its water coverage typically exceeds 3000 km² and even reaches 3500 km². The size of PL is similar to that of the Great Salt Lake in western America. At present, studies on the LSWT of PL mainly focus on the seasonal and interannual variations [32-34], while the spatial variations of LSWT in PL have rarely received attention. As early as 1989, Xu and Ouyang [32] used a research vessel to conduct a short-duration investigation for the spatial variation of LSWT in PL during daytime in July and found that the spatial difference of LSWT could exceed 1.5 °C, with the high LSWT in the middle of north of PL and low LSWT in the southwest of PL. However, the short-duration investigation and the lack of nighttime sampling limit the generalizability of the results. Moreover, the variations in the climate background and lake basin of PL may also alter the spatial distribution of LSWT in the lake. These suggest that the spatial variation of LSWT in PL is still unclear, e.g., whether the spatial distribution during the day is the same as that at night?

Some studies have shown that PL can influence regional precipitation, including enhancing crossed storms [35,36], weakening crossed storms [37,38], and producing isolated convection [11]. However, the spatial variation of LSWT in PL is still unclear, and its effects on regional precipitation are also unclear. Recently, with the development of satellite remote sensing technology, satellite-based land surface temperature, such as the Moderate Resolution Imaging Spectroradiometer (MODIS) products, has not only a large observational area but also a high spatial resolution and high accuracy. It has been widely applied to monitor the LSWT of lakes around the world. For example, the Great Salt Lake in North America [39], Qinghai Lake [26] and Hulun Lake in China [40], and Victoria Lake in Africa [41].

Therefore, in this study, we will use MODIS products to reveal the spatial variation of LSWT of PL. Subsequently, with the assistance of on-site observations, we will reconstruct a 3D (spatial and temporal) LSWT data of PL based on the spatial variation of MODIS LSWT, and feed the 3D LSWT data into a regional numerical weather model, with the aim of revealing the effect of spatial variation of LSWT on local precipitation. The remainder of this paper is organized as follows: Section 2 describes PL and the data used in this study, while the spatial variation characteristics of LSWT in PL are analyzed in Section 3. The effects of spatial variation of LSWT in PL on local precipitation are explored in Section 4, and the conclusion is given in Section 5.

II. Data and PL

A. Data and processing

This study employs the synthetic product of MODIS MOD09A1, which provides an estimate of the surface spectral reflectance across 7 bands of Terra satellite, to identify the water body of PL. The MOD09A1 data has a horizontal resolution of 500 m × 500 m and a temporal resolution of 8 d, in which band 4 (corresponding to the green wavelength) and band 6 (corresponding to the mid-infrared wavelength) are used to construct the identification index of the water body. The land surface temperature product MYD11A2 with the horizontal resolution of 1000 m × 1000 m and the temporal resolution of 8 d, which are produced by the Aqua satellite platform with the MODIS instrument, is employed to explore the spatial distribution of LSWT of PL. The MODIS MOD09A1 and MYD11A2 products are obtained from https://ladsweb.modaps.eosdis.nasa.gov, and their time ranges are from January 2003 to December 2023. It is noted that the MODIS MOD09A1 data in the PL region (i.e., the data serial number h28v06) are recorded by the Terra satellite at approximately 10:30 local solar time (LST) and 22:30 LST every eight days, while MYD11A2 data are recorded by the Aqua satellite at approximately 01:30 local solar time (LST) and 13:30 LST every eight days. The MODIS MOD09A1 and MYD11A2 products are stored in Hierarchical Data Format using the integerized sinusoidal (i.e., ISIN) projection. The MODIS Reprojection Tool (MRT) is utilized to decode and reproject these MODIS data into the geographic coordinates with a horizontal resolution of 1 km × 1 km.

The 1-h LSWT data with an accuracy of 0.1 °C in July from 2017 to 2019 at the Nanjishan (NJS) buoy station (Fig. 1b), which is built by Jiangxi Normal University, was applied to assist MYD11A2 in building 3D (spatial and temporal) LSWT in PL. The water depth of the buoy station in July is about 2 m, and the temperature sensor is about 10 cm away from the water surface. The monthly mean 2-m air temperature at 02:00 LST at Duchang (DC) and Yongxiu (YX) stations from 2003 to 2023 were used to analyze the longwave radiation difference and heat exchange between lake and air. The National Centers for Environmental Prediction (NCEP) Final (FNL) data from July-August 2020, with a horizontal resolution of 1° × 1° and a temporal resolution of 6 h, are applied to drive the Weather Research and Forecasting (WRF) model. The NCEP FNL data are obtained from https://rda.ucar.edu/datasets/ds083.2/index.html. The accumulated rainfall at 231 meteorological observational stations around PL and radar quantitative precipitation estimation (RQPE) with the horizontal resolution of 0.01° × 0.01° from 1 July to 31 August 2020 are used to assess the performance of the WRF model. The rainfall and RQPE data are obtained from the meteorological observatory of Jiangxi Province, China, and the RQPE is derived by the Gated Recurrent Unit neural network model [42].

B. PL

PL is located on the southern bank of the middle and lower reaches of the Yangtze River, in the northern part of Jiangxi Province, within the East Asian Monsoon zone (Fig. 1a). It is the largest freshwater lake and the second-largest lake in China. PL spans approximately 130 km from north to south, with a width ranging from 3 km to 75 km in the east-west direction, and an average width of 30 km during the wet season. PL is a relatively shallow lake with an average depth of about 6 m in the wet season [43], but the spatial distribution of water depth is not uniform. The lake basin presents an overall pattern with lower elevations in the north and middle and higher elevations

in the southwest and southeast. In the north and middle of PL, the altitudes of the lake basin are generally less than 10 m, and can even reach -6 m (Fig. 1b). However, the altitudes of the lake basin in the southwest and southeast of PL are normally more than 12 m or even 14 m (Fig. 1b). Moreover, there are some steep mountains with the altitude of over 500 m to the west and northwest of PL such as Lushan, Mufu Mountain, and Meiling, and some hills with an altitude of blow 300 m to the northeast of PL (Fig. 1b). Under the environmental condition of high temperature and humidity in the monsoon region, coupled with complex terrain, local convection occurs frequently over PL and its nearby areas in summer.

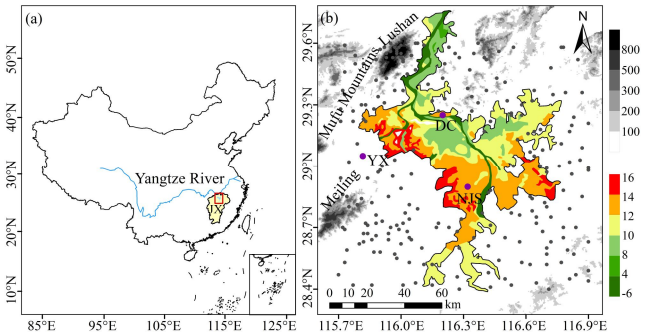

Fig. 1 (a) The location of PL in China, and (b) the altitudes of the lake basin of PL and its nearby areas. The blue line depicts the Yangtze River and the red rectangle represents the PL region in (a), and the JX denotes the Jiangxi Province. The small dots in (b) indicate the rain gauge stations, while the large purple dots represent the hydrological, meteorological or buoy stations.

PL is in fact a seasonal lake, and its water area closely links to the rainfall in Jiangxi and the water level of the Yangtze River. In order to reveal the mean variation of the water area of PL, the Modified Normalized Difference Water Index (MNDWI), which has been widely used to identify water pixels in satellite data [44], is selected to recognize the water body of PL. The expression of MNDWI [45] is as follows:

$$MNDWI = \frac{(Green - MIR)}{(Green + MIR)} \quad (1)$$

Where MIR denotes the MOD09A1 mid-infrared band reflectance, $Green$ denotes the green band reflectance, and the MNDWI value spans from -1 to 1. Generally, the MNDWI value of a pixel with water is greater than 0, while that with land is lower than 0. However, affected by mixed pixels (since the horizontal resolution of MOD09A1 is relatively low, it may often occur near lake shore), atmospheric correction, changes in water level caused by the movement of the land-water boundary, etc., the MNDWI values in some land points near water body may be also greater than 0. Therefore, setting appropriate thresholds can separate the water bodies from the land more effectively, reducing the uncertainty of water body identification near lake shores. Referencing the studies of Sun et al. [46] and Xie et al. [47], the MNDWI threshold to identify water points is set to 0.05 during January-April and October-December, and 0.1 during May-September.

The evolution of the averaged water area of PL in different months from 2003 to 2023 is shown in Fig. 2. It is noted that if a point is a water pixel in more than 50% of samples in a given month, this point is regarded as a water point, otherwise this point is considered a land point. There is an obvious seasonal variation in the water coverage of PL (Fig. 2). The large water areas of PL appear from June to August, with an area of above 3000 km^2, while the small water areas occur from October to February in the next year, with the area of below 1500 km^2. The largest water area of PL is present in July with an area of 3444 km^2, while the smallest water area is in January with an area of 1283.8 km^2. It can also be seen from Fig. 2 that the area of PL begins to expand obviously from April to June, and this period is just the main rainy season of Jiangxi province (Fig. 3a) and the rising season of the Yangtze River water level [48]. However, the water area of PL decreased rapidly in September and October (Fig. 2), which mainly resulted from the end of the rainy season of Jiangxi province (Fig. 3a) and the decline of water level in the Yangtze River [48]. The evolution of the water area of PL is similar to that of Dai et al.[49] and Xie et al. [47].

The water areas of PL are large (more than 3000 km^2) from June to August (Fig. 2), and the effects of PL on local precipitation/convection also mainly occur in this period [36]. Therefore, the spatial distribution of LSWT in PL from June to August is statistically analyzed in this paper. Since the water areas of PL in a month in different years may also vary, it is necessary to first identify whether a point/pixel is a water body when calculating the mean LSWT. If a point is a water body, the surface temperature of this point will be used to calculate the mean LSWT.

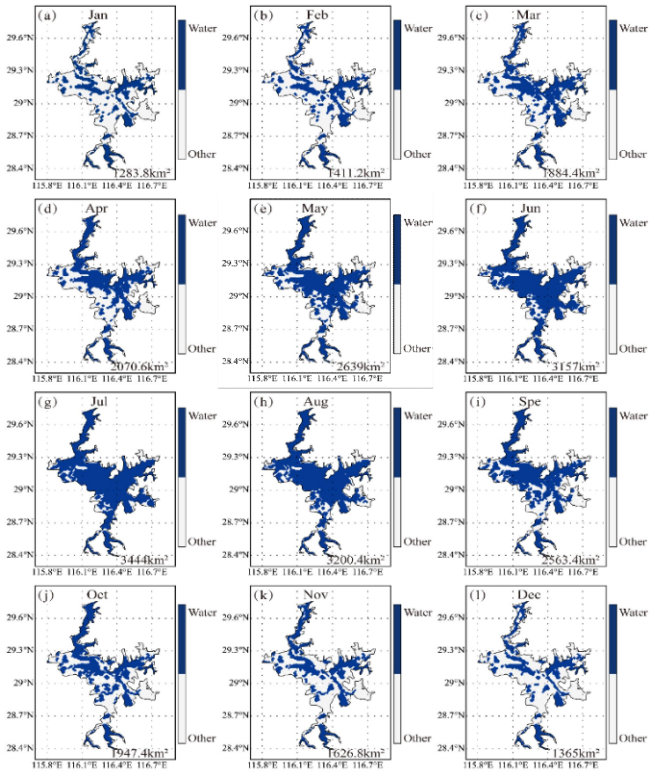

Fig. 2 The monthly mean water area of PL from 2003 to 2023.

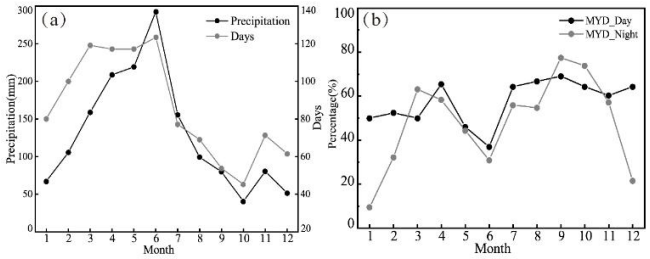

Fig. 3 (a) The monthly mean precipitation and rainy days at YX site, and (b) the ratio of valid MODIS LSWT data over PL from 2003 to 2023.

III. The Spatial Distribution of LSWT in PL

Fig. 4a shows the distribution of LSWT in PL at noon in June. The main high-temperature areas mainly occurred in the southwest, southeast, and northeast of PL, with the LSWT of above 27 °C, while the low-temperature areas mainly appeared in the middle and north of PL, with the LSWT of below 26.0 °C. The comparison between Fig. 1b and Fig. 4a reveals that the high-temperature areas are mainly located in the shallow-water areas of PL, while the low-temperature areas are mainly situated in the deep-water areas of PL, and the LSWT in the deep-water area can be 1.5 °C lower than that in a shallow-water area. The LWST distributions in the Great Lakes [28], Namco Lake [19], and Dianchi Lake [27] also appear to have a similar characteristic, with higher LSWT in shallow-water areas and lower LSWT in deep-water areas during the daytime. The distributions of LSWT of PL in the daytime of July and August are similar to that in June, with high-temperature areas in the southwest, southeast, and northeast of PL, and low-temperature areas in the middle and north of PL, except that the LSWT in July and August is about 2 °C higher than that in June. The spatial distribution of LSWT in PL is quite different from the finding of Xu and Ouyang [32] in that the middle of the north of PL is a high-temperature area, while the southwest of PL is a low-temperature area. This may be a result of the variations in the climate background of PL region and the lake basin of PL (e.g., the project of returning farmland to lakes was accomplished in 1998).

At night (i.e., 01:30 LST), the distribution of LSWT of PL (Fig. 4d) is roughly consistent with that at noon (Fig. 4a) in June, except that the LSWTs in southeast of PL are relatively low rather than high (Fig. 4d). In midsummer (i.e., July and August), the distributions of LSWT in PL at night are more consistent with those at noon, and the low-temperature area in the southeast of PL (i.e., Fig. 4a) is also switch to a high-temperature area (Fig. 4e-f). It is noted that due to the continued radiation cooling of PL from 01:30 LST to sunrise, this distribution does not fully represent the distribution of LSWT in PL during nighttime. Moreover, it also can be seen from Fig. 4 that in midsummer (Fig. 4b-c), the LSWTs near the shorelines of PL at noon are significantly warmer than those in other areas (especially on the north shorelines of PL), and such phenomenon does not occur in the night (Fig. 4e-f). This may be a result of land (with high surface temperature) contamination of water pixels near the lakeshore due to the relatively low horizontal resolutions of MODIS MYD11A2 and MOD09A1 products, causing the overestimation of LSWT. Reinart et al. [50] also discovered a similar phenomenon and indicated that the high LSWT near the shoreline of a lake may be induced by the warming of the adjacent land during the daytime.

In order to further examine the distribution of LSWT in PL at noon (13:30 LST) and night (01:30 LST), the spatial correlation is conducted between monthly mean LSWTs at noon and night. Since the north (i.e., latitude 29.3° N) and south (i.e., latitude < 28.7° N) of PL are narrow (Fig. 4a), LSWT data may be more heavily affected by the nearby land. Therefore, the data of LSWTs in the large central water area of PL (i.e., 28.7°N ≤latitude≤29.3°N) is used to calculate the spatial correlation. Moreover, the LSWT data near the shoreline of PL are also excluded, aiming to further reduce the effect of land contamination in the daytime [50]. Results show that the correlation coefficients in June, July, and August are 0.11, 0.41, and 0.23, respectively, all of which passed the reliability test of 99%. This further confirms the positive correlation relationship between LSWTs at noon and night in summer, especially for July and August.

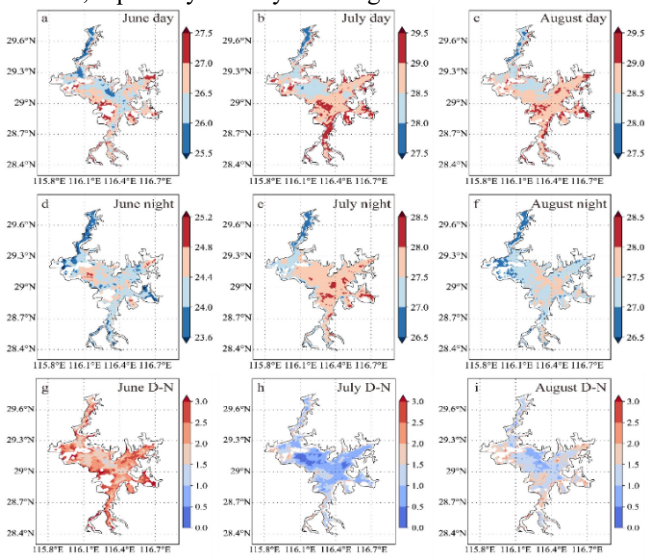

Fig. 4 The distribution of monthly mean LSWT (°C) of PL at daytime (13:30 LST, a-c), nighttime (1:30 LST, d-f) from 2003 to 2023, and their difference (daytime-nighttime).

The above analysis reveals that the spatial distribution of LSWT in PL is similar between noon (13:30 LST) and night (01:30 LST), characterized by high-temperature areas predominantly located in the southwest, south, and northeast regions, and low-temperature areas concentrated in the central and northern parts of the lake. Interestingly, this pattern contrasts with other lakes, such as Dianchi Lake, where the LSWT distributions at noon and night are roughly opposite [27]. In fact, even for PL, the LSWT distributions during autumn and winter exhibit an opposite trend between noon and night (not shown), with spatial correlation coefficients of approximately -0.2. This raises a question: why does PL exhibit a similar spatial distribution of LSWT between noon

and night during summer?

Solar radiation serves as the primary energy source to drive LSWT in a lake due to its high energy input. During the daytime, different areas of PL with varying water depths receive similar solar radiation. Since the water depth of PL is relatively shallow, solar radiation can penetrate the water body and reach the lake bottom. As a result, the soil in the lake bottom can also be directly heated by solar radiation, and the heated thickness of the soil is usually concentrated within a relatively thin layer [51]. Therefore, in shallow-water regions with low water column, the solar radiation can noticeably warm up not only the water body but also the soil of the lake bottom, causing a higher LSWT due to the water mixing and the heat diffusion from the bottom. In contrast, in deeper-water areas, the solar radiation is distributed over a larger volume of water and that arrived at the bottom is relatively weak, resulting in a lower LSWT. This mechanism explains the LSWT distribution in PL at noon (Fig. 4a-c).

However, in the nighttime, solar radiation disappears, and the energy budget of lake surface is as follow:

$$L - H - E = G \tag{2}$$

Where L the net longwave radiation, H and E are sensible heat and latent heat flux, and G is the heat transfer between lake surface and water body [8]. The terms of L and H are calculated by the following formulas [52,53]:

$$L = \varepsilon_a \sigma T_a - \varepsilon_s \sigma T_s \tag{3}$$

$$H = \rho C_h U (T_s - T_a) \tag{4}$$

Where T_s and T_a are LSWT and air temperature, respectively. ε_a and ε_s are the emissivity of atmosphere and lake (normally, the former is smaller than the latter). ρ is the air density, σ is the Stefan-Boltzmann constant, U is the horizontal wind speed, and C_h is the heat exchange coefficient. It can be seen from Eq. (2)-(4) that the temperature difference between lake surface and air play an important role in the energy budget. If the $T_s > T_a$, $L < 0$ and $H > 0$, resulting in a quick loss of energy in a lake and a rapidly decrease in LSWT. In contrast, if $T_s < T_a$, $H < 0$ and L is small negative value or may even greater than 0. In this case, the lake losses energy slowly or may even gains energy from atmosphere, resulting in a slow loss of energy in a lake and a slowly decline in LSWT. Overall, T_s-T_a is a key factor to affect the rate of cooling of LSWT, and the larger the T_s-T_a, the stronger the cooling of LSWT.

Fig. 5 illustrates the monthly variations in the 2-m air temperature at DC (located north of PL and upstream of PL during winter) and YX (situated southwest of PL and upstream of PL during summer), as well as the monthly mean LSWT of PL at night (01:30 LST). The 2-m air temperatures at DC and YX are nearly identical and are significantly lower than the LSWT of PL from January to May and October to December. This suggests that the large T_s-T_a accompanies a rapid loss of energy in PL at night during winter, which results in a rapid cooling (especially for the shallow-water area), ultimately leading to an opposite spatial distribution of LSWT between noon (13:30 LST) and night (01:30 LST). However, in summer, due to the influence of the Western Pacific Subtropical High, the 2-m air temperature rises markedly and approaches or even slightly exceeds the LSWT of PL at night (01:30 LST), with a small T_s-T_a. Xu and Ouyang [32] also indicated the T_s-T_a of PL in summer is obviously smaller than that in winter based on the hydrological observational data at 08:00 LST. Therefore, at night in summer, the loss of energy in PL is slow, and the cooling of PL is slow, finally resulting in a similar spatial distribution of LSWT between noon (13:30 LST) and night (01:30 LST).

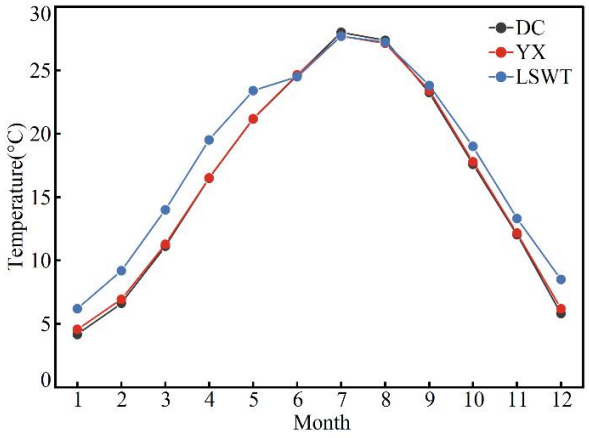

Fig. 5 The monthly mean 2-m air temperature at DC and YX, and the LSWT of PL at nighttime (i.e., 01:30 LST) from 2003 to 2023.

IV. SIMULATION STUDY OF THE EFFECT OF LSWT IN PL ON REGIONAL PRECIPITATION

Fig. 4g-i shows the diurnal range of LSWT (i.e., the difference in LSWT between noon and night) in PL. The diurnal ranges in the main body of PL during July and August are generally less than 1.5 ℃, which is significantly smaller than those in June (diurnal ranges are usually more than 2 ℃ or even 2.5 ℃). However, Wang [54] and Yang et al. [55] utilized site-observation data of LSWT to discover that the diurnal range of LSWT in water bodies tended to be larger on sunny days, and lower on rainy and cloudy days [54,55]. This raises the question: why is the diurnal range of MODIS LSWT notably larger in June, which has more rainy or cloudy days, compared to July and August, which have more sunny days? Fig. 3b reveals that the valid ratio of MODIS LSWT data at night (noon) in June is less than 30% (40%), significantly lower than those in July and August. This is primarily due to the higher frequency of rainy and cloudy days in June (Fig. 3a). Moreover, the matching rate of MODIS LSWT data between noon and night (i.e., the proportion of days with valid MODIS LSWT data at both noon and night over PL region) is also low, at approximately 36%, which is about half of those in July and August. The high mismatch rate of MODIS LSWT data between noon and night in June likely contributes to the larger diurnal range observed in Fig. 4g, as it may inadvertently incorporate daily variations or even annual variations. Therefore, the diurnal range of LSWT of PL in June may not accurately represent the actual diurnal variation. Consequently, the subsequent numerical simulations and analyses

will focus on July and August. It is worth noting that the high mismatch rate of MODIS LSWT data between noon and night in June does not affect obviously the spatial distribution of LSWT.

A. Model configuration

This study utilizes the WRF model version 4.2, released in April 2021, to simulate the effect of LSWT in PL on regional precipitation. Three one-way nested domains are used in the model, with the outermost domain (i.e., the largest domain) centered at the point (28.5°N, 116.2°E). The three domains have 301 (281), 241 (241), and 181 (171) grids in the east-west (south-north) direction, and the corresponding grid spacing is 9 km, 3 km, and 1 km, respectively. The configuration of the physical schemes in the model is the same as that in the studies [11,23] and is as follows: the Grell-Freitas scheme is applied in the outermost domain, and no cumulus parameterization schemes are used in the middle and innermost domains. Since the advantages of simulating precipitation in the lake region [56-58], the Thompson microphysics scheme and the unified Noah land-surface scheme are adopted in the three domains. The schemes for the planetary boundary layer and longwave radiation are set to the Rapid Radiative Transfer Model and the Yonsei University schemes, respectively. The initial and lateral boundary conditions of the model come from the 6-hourly NCEP FNL data.

B. Experimental design

To investigate the influence of LSWT in PL on regional precipitation, two sets of experiments were designed. The first is the non-update (NOUP) experiment, where the LSWTs of PL are directly derived from the WRF model and remain constant in both space and time. In the NOUP experiment, the LSWT of PL is fixed at approximately 28°C for July and August. The second experiment, referred to as the update (UP) experiment, incorporates both the spatial and temporal variations of LSWT in PL. In the UP experiment, the LSWTs in the innermost domain are derived from a combination of the spatial distribution of MODIS LSWT and the temporal evolution (diurnal variation) of in-situ observations at the Nanjishan (NJS) station (Fig. 6). The LSWT changes in the UP experiment are implemented by updating the bottom boundary conditions (i.e., setting sst_update=1 in the WRF model), with an update frequency of 1 hour. It is noted that the WRF model settings in the NOUP and UP experiments are identical, except for the treatment of LSWT in the innermost domain. Both the NOUP and UP experiments were conducted 62 times from 1 July to 31 August 2020. Each simulation started at 20:00 LST on the previous day and ended at 08:00 LST on the following day, spanning a total of 36 hours. The first 12 hours were allocated as spin-up time for the model, while the simulations from the subsequent 24 hours were used for verification and analysis.

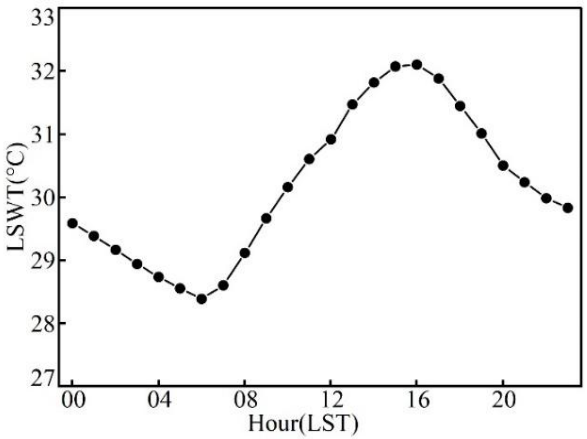

Fig. 6 The Hourly LSWT data in July at NJS averaged from 2017 to 2019.

Specifically, the LSWTs of PL in the UP experiment are calculated by the following formula:

$$T(i,j,t) = T_M(i,j) - A(i,j) + 2A(i,j)\frac{T_O(t) - T_O(t=6)}{T_O(t=16) - T_O(t=6)} \quad (5)$$

$$A(i,j) = \left(T_{MD}(i,j) - T_{MN}(i,j)\right)\frac{T_O(t=16) - T_O(t=6)}{T_O(t=13{:}30) - T_O(t=01{:}30)} \quad (6)$$

$$T_M(i,j) = \frac{T_{MD}(i,j) + T_{MN}(i,j)}{2} \quad (7)$$

Where T_{MD} (T_{MN}) indicates the averaged MODIS LSWT at noon (night) from July to August from 2003 to 2023. In other words, T_{MD} is the average of Fig. 4b and Fig. 4e, while T_{MN} is the average of Fig. 4c and Fig. 4f. T_M is the average of MODIS LSWT between noon and night, and T_O is the mean hourly LSWT at NJS (i.e., Fig. 6). A represent the amplitude of the diurnal variation of MODIS LSWT. It can be seen from Eq. (5)-(7), the restructured LSWT includes not only the spatial distribution information that is similar to that of MODIS LSWT, but also the diurnal variation information that is analogous to that of in-situ observation.

C. Results

1) Precipitation: The distribution of the observational accumulated precipitation in the PL region from July to August 2020 is shown in Fig. 7a. Clearly, the large precipitation is mainly located to the southwest and northeast of PL, with the maximum precipitation exceeding 700 mm. In the south and southeast of PL, most of the stations have accumulated precipitation of less than 400 mm or even 300 mm. Due to the lack of observation stations over PL, it is difficult to reveal the accurate distribution of precipitation over PL in Fig. 7a. To address this problem, the RQPE is also calculated by the Z-R relationship of $Z=79R^{1.68}$, which is obtained by the optimal method based on the observations of radar reflectivity and precipitation [42]. Fig. 7b shows the distribution of the accumulated RQPE during July-August 2020. The distributions of RQPE (Fig. 7b) are quite similar to that of the observation in the rain gauge (i.e., Fig. 7a), with the large precipitation situated to the southwest and northeast of PL, and the small precipitation located to the south and southeast of PL. This also verifies the accuracy of RQPE. Importantly, Fig. 7b shows that the

precipitation over PL (especially in the southeast of PL) is smaller than that to the north, west, and east sides of PL, suggesting that PL may decrease the precipitation over it. It is noted that the very small RQPE near the NC radar site (i.e., the area within the red circle in Fig. 7b) is mainly induced by the radar blind zone in the short range.

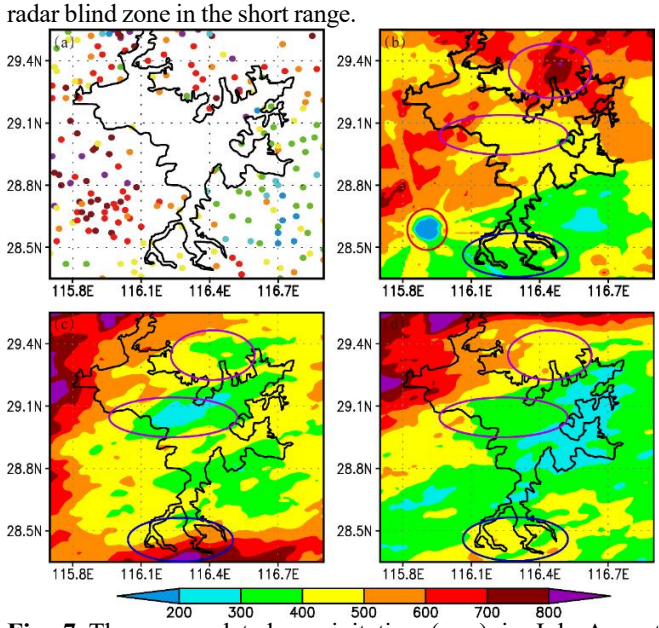

Fig. 7 The accumulated precipitation (mm) in July-August 2020 for (a) the observation in the rain gauge, (b) the RQPE, (c) the simulation of the NOUP experiment and (d) the simulation of the UP experiment.

The simulated precipitation of the NOUP experiment is shown in Fig. 7c. The large precipitation is mainly situated to the northwest and south of PL, with the maximum precipitation exceeding 700 mm or even reaching 800 mm, while the small precipitation is mainly located in the middle, north, and southeast of PL, with the minimum precipitation below 300 mm or even 200 mm. Compared with the observations (i.e., Fig. 7a-b), the simulated precipitation in the middle and north of PL (i.e., the areas within the purple circles) is obviously weak, with a decrease of about 200 mm. However, on the south side of PL, the NOUP experiment simulates precipitation exceeding 700 mm, which is markedly greater than that of the observations, with an increase of about 400 mm. Apparently, the NOUP experiment does not simulate the distribution of precipitation in the PL region well. In the UP experiment, the simulated precipitation in the middle and north of PL (the purple circles in Fig. 7d) has obviously increased compared to the NOUP experiment, while the simulated precipitation in the south of PL (the blue circle in Fig. 7d) has decreased remarkably, with a decrease by about 300 mm. The distribution of precipitation simulated by the UP experiment is closer to that of the observation. Clearly, the UP experiment has demonstrated better performance in simulating precipitation in the PL region than the NOUP experiment. This indicates that introducing the temporal and spatial variations of LSWT in the WRF model can improve the simulation capability of precipitation in the PL region.

2) Atmospheric instability: Although precipitation is a complex physical process of the atmosphere, it is generally formed by the lifting and condensation of air rich in water vapor. Usually, precipitation can be divided into systematic precipitation with a large scale and convective precipitation with a relatively small scale. The underlying surface with a relatively small scale often cannot significantly affect the systematic precipitation, but can evidently influence convective precipitation. Also, the precipitation in the PL region in the summer (especially from July to August) is mainly convective precipitation. Johns and Doswell [59] indicated that the development of convective precipitation needs to meet several basic ambient conditions, such as low-level uplifting movement which is the key factor in determining whether the near-surface air can be uplifted, and atmospheric instability which can promote the air uplifted from the near surface to continue to rise in the middle and lower troposphere. The convective available potential energy (CAPE) is an important index for evaluating atmospheric instability and reflects the overall instability of the atmosphere. Therefore, it has been widely used to forecast or diagnose convective storms or precipitation [11,16,60,61]. Usually, a large CAPE usually indicates that strong convection or precipitation is likely to develop.

Fig. 8a-b illustrates the CAPEs of the NOUP experiment and the UP experiment averaged from July to August 2020. The mean CAPEs of the NOUP and UP experiments are relatively large over PL and its nearby areas, with a value above 1000 J kg^{-1} (except for the area near Lushan), indicating that convective precipitation is likely to develop in the PL region during this period. However, there is an obvious difference in the distribution of CAPEs. Specifically, in the NOUP experiment with the default LSWT (Fig. 8a), the CAPEs over PL are significantly smaller than those elsewhere (except for the area near Lushan). However, in the UP experiment with the updated LSWT, the CAPEs over PL are significantly greater than those of elsewhere (Fig. 8b). Fig. 8c shows the difference in CAPE between the two experiments. It is clear that the CAPEs over PL have a remarkable increase after updating the LSWT in the WRF model, with a maximum increment of more than 200 J kg^{-1}, while the CAPEs in the area around PL have a decrease of 0-150 J kg^{-1}. By comparing Fig. 7 and Fig. 8, it can be seen that in the areas with the rise of precipitation in the UP experiment compared to the NOUP experiment, the CAPEs increase significantly (i.e., the area over PL) or change slightly (i.e., the area north of PL), but in the areas with the decline of precipitation, the CAPEs decrease remarkably (i.e., the area south of PL). This suggests that the increased CAPE contributes to the rise of precipitation over PL, and the decreased CAPE contributes to the decline of precipitation to the south of PL.

In fact, CAPE is the integrated amount of work that the upward buoyancy force would perform on an air parcel if it rose vertically through the entire atmosphere [62] and is significantly affected by the near-surface air temperature and humidity. The changes in LSWT in the UP experiment (compared to those in the NOUP experiment) can directly affect the near-surface air temperature and humidity through

the exchanges of water vapor and heat between PL and its overlying air [11]. Subsequently, the near-surface air over PL, which has been affected by the PL, can be outwardly advected and diffused under the low-level wind, finally affecting the near-surface air temperature and humidity over the nearby areas of PL. This is responsible for the changes in CAPE over PL and its nearby areas in the NOUP and UP experiments.

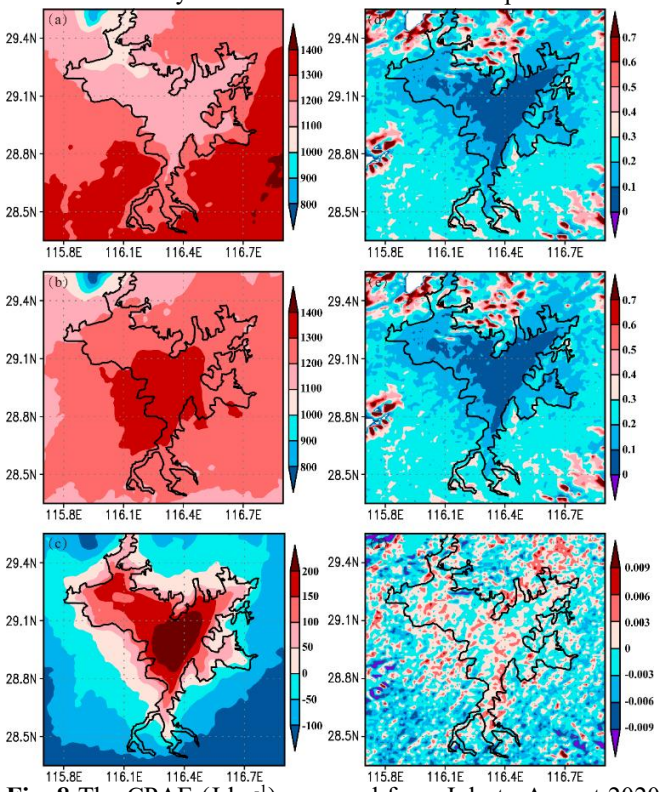

Fig. 8 The CPAE (J kg^{-1}) averaged from July to August 2020 in (a) NOUP and (b) UP experiments, and (c) their difference (i.e., UP-NOUP). (d-f) are the same as (a-c), except for the upward motion with a velocity of exceeding 0.1 m s^{-1}.

3) Low-level uplifting: Although CAPE is an important index to indicate whether strong convective precipitation is likely to develop, the release of CAPE requires that the near-surface air mass can be uplifted above the level of free convection (LFC). If an air parcel with a large CAPE is not uplifted above the LFC, the CAPE cannot be released, and convective precipitation is also not likely to develop. However, whether the near-surface air parcel with a large CAPE can be lifted above the LFC is closely related to the intensity of the uplift movement of low-level air. Therefore, the low-level uplift movement is also a key factor for the development of convective precipitation [59], and the low-level uplift movement is related to the underlying surface [63,64].

Fig. 8d shows the mean upward velocity with an intensity of more than 0.1 m s^{-1} at 975 hPa in the NOUP experiment. Apparently, the strong uplift movement occurs mainly near the topography, indicating the uplift effect of topography on air at a low level. This is also the main reason why topography produces precipitation under certain conditions. It can also be seen from Fig. 8d that the mean upward velocities over PL are obviously smaller than those elsewhere, which may be induced by the small surface roughness over lakes. The distribution of vertical velocity exceeding 0.1 m s^{-1} in the UP experiment (Fig. 8e) is quite similar to that in the NOUP experiment (Fig. 8d), and it is very difficult to distinguish the discrepancy between them with the naked eye. Therefore, the difference in the mean upward velocity with an intensity exceeding 0.1 m s^{-1} between the UP experiment and the NOUP experiment is calculated and shown in Fig. 8f. After updating the LSWT in PL, the 975 hPa upward motions over PL and its northeast side are remarkably increased, while they are dominated by the weakened upward motions to the south of PL. This implies that the increased upward motion over PL and its northeast side contributes to the enhancement of precipitation, while the weakened upward motion to the south of PL contributes to the weakening of precipitation in the UP experiment.

According to the above analysis, it can be suggested that the decrease in precipitation to the south of PL is jointly induced by the weakening of upward motion and atmospheric instability (i.e., CAPE) in the UP experiment, while the increase in precipitation over PL is jointly induced by the enhancements in upward motion and atmospheric instability. However, the increase of precipitation in the northeast of PL mainly results from the enhanced upward motion in the UP experiment.

V. Conclusion

Based on the MODIS LSWT and MOD09A1 products from 2003-2023, this study analyzes and reveals the spatial variations of LSWT in PL. Combining the spatial distribution characteristics of MODIS LSWT and the temporal evolution of LSWT in NJS buoy station, a 3D (horizontal and time) dataset of LSWT of PL during July-August is restructured. Then, the restructured 3D dataset of LSWT is introduced into the WRF model to simulate the precipitation during July-August 2020 over PL region, improving the accuracy of the simulated precipitation over PL region.

During summer (June-August), the high-LSWT areas at noon are mainly located at the east and south of PL where the water is relatively shallow, while the low-LSWT areas are mainly situated in the middle and north of PL where the water is relatively deep. At night, the distribution of LSWT in PL is roughly consistent with that at noon. This is obviously different from that of PL in the winter season and other lakes such as Dianchi (Wang et al., 2021). Corresponding diagnosis suggests that this is mainly induced by the high air temperature at night over PL region under the control of the Western Pacific Subtropical High. The air with high temperature at night can prevent the cooling of PL by enhancing the downward longwave radiation of the atmosphere and reducing the heat transport from lake to air, finally making the spatial distribution of LSWT at night (01:30 LST) roughly consistent with noon.

In order to reveal the effects of spatial variation of LSWT in PL on regional precipitation, the non-update (NOUP) experiment with the default LSWT in the WRF model and the

update (UP) experiment with the restructured 3D LSWT were conducted. Results show that compared to the NOUP experiment, the UP experiment obviously improves the simulation of the precipitation in PL region. Diagnoses show that the effects of LSWT on local precipitation are accomplished by adjusting the atmospheric instability and upward motion at the low level. Concretely, the decrease in precipitation to the south of PL is jointly induced by the weakening of upward motion and atmospheric instability (i.e., CAPE) in the UP experiment, while the increase in precipitation over PL is jointly induced by the enhancements in upward motion and atmospheric instability. However, the increase of precipitation in the northeast of PL mainly results from the enhanced upward motion in the UP experiment.

Although this study has revealed the spatial variation characteristics of LSWT in PL, it is conducted by MODIS land surface temperature products. Since the MODIS products are obtained based on optical remote sensing, the LSWT in PL is only available on sunny days without clouds and rainfall. Therefore, the spatial distribution of LSWT in PL may not completely represent the distribution on cloudy and rainy days. Moreover, MODIS MYD11A2 data is recorded at 01:30 LST and 13:30 LST, and it may not commendably reflect the maximum and minimum of LSWT in PL. Therefore, more site observation and radar remote sensing data are required to discover the spatial distributions of LSWT in PL. Since the restructured 3D LSWT in PL is based on the spatial distribution of MODIS LSWT and the diurnal variation of NJS-site observation, it doesn't include daily variation and may not reflect the spatial distribution of LSWT on rainy and cloudy days. In addition, the diurnal variation of different points in PL may also not be the same as that in NJS station. Therefore, there is still some room to further improve the accuracy of the simulated precipitation in the PL region. Especially, 3D lake models, which are closer to reality as they can simulate the thermal dynamics in the longitudinal, lateral, and vertical directions and used in other lakes [65], should be fully coupled into the atmosphere model to improve the simulations of precipitation in the PL region.

Conflict of Interest

The authors declare that they have no known competing financial interests or personal relationships that could have appeared to influence the work reported in this paper.

References

[1] S. Sharma, D. K. Gray, J. S. Read et al., "A global database of lake surface temperatures collected by in situ and satellite methods from 1985–2009," *Scientific Data*, vol. 2, no. 1, pp. 1-19, 2015, doi: 10.1038/sdata.2015.8.

[2] R. I. Woolway, M. T. Dokulil, and W. Marszelewski et al., "Warming of Central European lakes and their response to the 1980s climate regime shift," *Climatic Change*, vol. 142, no. 3-4, pp. 505-520, 2017, doi: 10.1007/s10584-017-1966-4.

[3] Y. Li, Q. Zhang, and J. Yao et al., "Hydrodynamic and hydrological modeling of the Poyang Lake catchment system in China," *Journal of Hydrologic Engineering*, vol. 19, no. 3, pp. 607-616, 2014.

[4] M. Chen, Y. Zhang, and J. Li et al., "The effects of temperature differences on anaerobic degradation of submerged macrophytes litter in lake sediments," *Acta Scientiae Circumstantiae*, vol. 40, no. 8, pp. 3013-3019, doi: 10.13671/j.hjkxxb.2019.0386. (in Chinese)

[5] J. C. Ho, A. M. Michalak, "Exploring temperature and precipitation impacts on harmful algal blooms across continental US lakes," *Limnology and Oceanography*, vol. 65, no. 5, pp. 992-1009, May. 2020, doi: 10.1002/lno.11365.

[6] D. B. Bunnell, S. A. Ludsin, and R. L. Knight et al., "Consequences of changing water clarity on the fish and fisheries of the Laurentian Great Lakes," *Canadian Journal of Fisheries and Aquatic Sciences*, vol. 78, no. 10, pp. 1524-1542, 2021, doi: 10.1139/cjfas-2020-0376.

[7] J. Wan, D. Lu, and F. Liu, "Summer temperature field and its temperature effect in Poyang Lake," *Quart. J. Appl. Meteorol*, vol. 5, pp. 374-379, 1994. (in Chinese)

[8] Y. Wu, A. Huang, and Lazhu et al., "Improvements of the coupled WRF-lake model over lake Nam Co, central Tibetan plateau," *Climate Dynamics*, vol.55, pp. 2703-2724, Aug. 2020, doi: 10.1007/s00382-020-05402-3.

[9] Y. Wang, Y. Gao, and H. Qin, "Spatiotemporal characteristics of lake breezes over Lake Taihu, China," *Journal of Applied Meteorology and Climatology*, vol. 56, no. 7, pp. 2053-2065, Jul. 2017, doi: 10.1175/JAMC-D-16-0220.1.

[10] X. Yang, Y. Lu, and J. Wen et al., "Numerical simulation of typical characteristics of land surface water-heat exchange over Gyaring Lake and Ngoring Lake in summer," *Plateau Meteorology*, vol. 41, no. 1, pp. 143-152, 2022, doi: 10.7522/j.issn.1000-0534.2020.00090. (in Chinese).

[11] H. Zou, M. Tian, and Z. Bin et al., "Impacts of spatiotemporal variation in lake surface temperature on convection over Poyang Lake," *Journal of Atmospheric and Solar-Terrestrial Physics*, vol. 245, 2023, doi: 10.1016/j.jastp.2023.106048.

[12] T. J. Miner, and J. M. Fritsch, "Lake-effect rain events," *Monthly Weather Review*, vol. 125, no. 12, pp. 3231-3248, 1997, doi: 10.1175/1520-0493(1997)125<3231:LERE>2.0.CO;2.

[13] D. A. Kristovich, and M. L. Spinar, "Diurnal variations in lake-effect precipitation near the western Great Lakes," *Journal of Hydrometeorology*, vol. 6, no. 2, pp. 210-218, 2005, doi: 10.1175/JHM403.1.

[14] N. F. Laird, J. Desrochers, and M. Payer, "Climatology of lake-effect precipitation events over Lake Champlain," *Journal of applied meteorology and climatology*, vol. 48, no. 2, pp. 232-250, 2009, doi: 10.1175/2008JAMC1923.1.

[15] N. F. Laird, A. M. Bentley, and S. A. Ganetis et al., "Climatology of lake-effect precipitation events over Lake Tahoe and Pyramid Lake," *Journal of Applied Meteorology and Climatology*, vol. 55, no. 2, pp. 297-312, 2016, doi: 10.1175/JAMC-D-14-0230.1.

[16] Z. Zhao, A. Huang, and W. Ma et al., "Effects of Lake Nam Co and surrounding terrain on extreme precipitation over Nam Co basin, Tibetan Plateau: A case study," *Journal of Geophysical Research: Atmospheres*, vol. 127, no. 10, 2022, doi: 10.1029/2021JD036190.

[17] Y. Wu, A. Huang, and B. Yang et al., "Numerical study on the climatic effect of the lake clusters over Tibetan Plateau in summer," *Climate Dynamics*, vol. 53, pp. 5215-5236, 2019, doi: 10.1007/s00382-019-04856-4.

[18] J. Sun, W. Hu, and N.Wang, et al., "Eddy covariance measurements of water vapor and energy flux over a lake in the Badain Jaran Desert, China," *Journal of Arid Land*, vol. 10, pp. 517-533, 2018, doi: 10.1007/s40333-018-0057-3.

[19] J. Wang, L. Huang, and J. Ju et al., "Spatial and temporal variations in water temperature in a high-altitude deep dimictic mountain lake (Nam Co), central Tibetan Plateau," *Journal of Great Lakes Research*, vol. 45, pp. 212-223, 2019, doi: 10.1016/j.jglr.2018.12.005.

[20] G. Liu, W. Ou, and Y. Zhang et al., "Validating and mapping surface water temperatures in Lake Taihu: Results from MODIS land surface temperature products," *IEEE Journal of Selected Topics in Applied Earth Observations and Remote Sensing*, vol. 8, no. 3, pp. 1230-1244, 2015, doi: 10.1109/JSTARS.2014.2386333.

[21] D. M. Carpenter, "The lake effect of the Great Salt Lake: Overview and forecast problems," *Weather and Forecasting*, vol. 8, no. 2, pp. 181-193, 1193. Doi: 10.1175/1520-0434(1993)008<0181:TLEOTG>2.0.CO;2

[22] D. M. Wright, D. J.Posselt, and A. L. Steiner, " Sensitivity of lake-effect snowfall to lake ice cover and temperature in the Great Lakes region," *Monthly Weather Review*, vol. 141, no. 2, pp. 670-689, 2013, doi: 10.1175/MWR-D-12-00038.1.

[23] H. Zou, S. Wu, and J. Shan, "Sensitivity of lake-effect convection to the lake surface temperature over Poyang Lake in China," *Journal of*

Meteorological Research, vol. 36, no. 2, pp. 342-359, 2022, doi: 10.1007/s13351-022-1142-2.

[24]T. E. Workoff, D. A. Kristovich, and N. F. Laird et al., "Influence of the Lake Erie overlake boundary layer on deep convective storm evolution," *Weather and Forecasting*, vol. 27, no. 5, pp. 1279-1289, 2012, doi: 10.1175/WAF-D-11-00076.1.

[25]Z. Yu, K. Yang, and Y. Luo et al., "Lake surface water temperature prediction and changing characteristics analysis - A case study of 11 natural lakes in Yunnan-Guizhou Plateau," *Journal of Cleaner Production*, vol. 276, pp. 122689, 2020, doi: 10.1016/j.jclepro.2020.122689.

[26]K. Song, M. Wang, and J. Du et al., "Spatiotemporal variations of lake surface temperature across the Tibetan Plateau using MODIS LST product," *Remote Sensing*, vol. 8, no. 10, pp. 854, 2016, doi: 10.3390/rs8100854.

[27]Y. Wang, Y. Luo, and W. Tan et al., "Analysis of temporal and spatial variation process of Dianchi Lake surface water temperature based on MODIS remote sensing images," *In IOP Conference Series: Earth and Environmental Science*, vol. 658, no. 1, pp. 012005, 2021, doi: 10.1088/1755-1315/658/1/012005.

[28]C. G. Fichot, K. Matsumoto, and B. Holt et al., "Assessing change in the overturning behavior of the Laurentian Great Lakes using remotely sensed lake surface water temperatures," *Remote Sensing of Environment*, vol. 235, 2019, doi: 10.1016/j.rse.2019.111427.

[29]P. T. Strub, and T. M. Powell, "Surface temperature and transport in Lake Tahoe: Inferences from satellite (AVHRR) imagery," *Continental Shelf Research*, vol. 7, no. 9, pp. 1001-1013, 1987, doi: 10.1016/0278-4343(87)90096-3.

[30]M. T. Dokulil, E. de Eyto, and S. C. Maberly et al., "Increasing maximum lake surface temperature under climate change," *Climatic Change*, vol. 165, no. 3, p. 56, 2021, doi: 10.1007/s10584-021-03085-1.

[31]J. Austin, and S. Colman, "A century of temperature variability in Lake Superior," *Limnology and Oceanography*, vol. 53, no. 6, pp. 2724-2730, 2008, doi: 10.4319/lo.2008.53.6.2724.

[32]H. Xu, and X. Ouyang, "The water temperature of Poyang Lake," *Oceanology and Limnology Sinica*, vol. 20, pp. 343–353, 1989. (in Chinese)

[33]J. Wang, T. Liu, and X. Liu et al., "Analysis of water temperature between automatic thermometer and human observation values in Poyang Lake," *Journal of Water Resources Research*, vol. 5, pp. 516-520, 2016, doi: 10.12677/JWRR.2016.55060. (in Chinese)

[34]Q. Wu, "Study on water temperature distribution of Poyang Lake and water age of Poyang Lake influenced by hydraulic project," M.S. thesis, Nanchang University, Nanchang, 2017. (in Chinese)

[35]A. Xu, C. Ye, and L. Ouyang et al., "The diagnostic analysis of the track and precipitation of typhoon "RANANIM" after landfall," *Journal of Tropical Meteorology*, vol. 12, no. 2, pp. 189-192, 2016. (in Chinese)

[36]H. Zou, "Statistical Analysis and Case Study of Lake-Effect Precipitation over Poyang Lake," Ph.D. dissertation, Lanzhou University, Lanzhou, 2020. (in Chinese)

[37]M. Fu, Y. Zheng, and H. Zou et al., "Analysis on weakening process of convective system passing over Poyang Lake in summer," *Plateau Meteorology*, vol. 32, no. 3, pp. 865-873, 2013, doi: 10.7522/j.issn.1000-0534.2012.00080.

[38]C. Fu, Y. Chen, and S. Yin et al., "Numerical simulation of physical process of precipitation intensity weakening in Poyang Lake," *Meteorological Monthly*, vol. 47, no. 1, pp. 24-35, 2021, doi: 10.7519/j.issn.1000-0526.2021.01.003.

[39]E. T. Crosman, and J. D. Horel, "MODIS-derived surface temperature of the Great Salt Lake," *Remote Sensing of Environment*, vo. 113, no. 1, pp. 73-81, 2009, doi: 10.1016/j.rse.2008.08.013.

[40]R. Wang, and Z. Niu, "Characteristics of changes in lake temperature in China and their response to climate change," *China Environmental Science*, vol. 40, no. 2, pp. 780-788, 2020. (in Chinese)

[41]G. Wu, C. Chen, Y. Liu, "Developing a high-resolution seamless surface water extent time-series over Lake Victoria by integrating MODIS and Landsat data," *Remote Sensing*, vol. 15, no. 14, pp. 3500, 2023, doi: 10.3390/rs15143500.

[42]H. Zou, S. Wu, and M. Tian, "Radar quantitative precipitation estimation based on the gated recurrent unit neural network and echo-top data," *Advances in Atmospheric Sciences*, vol. 40, no. 6, pp. 1043-1057, 2023b, doi: 10.1007/s00376-022-2127-x.

[43]D. Shankman, B. D. Keim, and T. Nakayama et al., "Hydroclimate analysis of severe floods in China's Poyang Lake region," *Earth Interactions*, vol. 16, no. 14, pp. 1-16, 2012, doi: 10.1175/2012EI000455.1.

[44]N. Zhang, W. Wang, and Y. Wang et al., "Estimate the area of the Poyang Lake using satellite remote sensing data and analyze its relationship with water level," *Remote Sensing Technology and Application*, vol. 27, no. 6, pp. 947-953, 2012.

[45]H. Xu, "A study on information extraction of water body with the modified normalized difference water index (MNDWI)," *JOURNAL OF REMOTE SENSING-BEIJING-*, vol. 9, no. 5, pp. 595, 2005, doi: 10.11834/jrs.20050586. (in Chinese)

[46]F. Sun, and R. Ma, "Hydrologic changes of Poyang Lake based on radar altimeter and optical sensor," *Acta Geographica Sinica*, vol. 75, no. 3, pp. 544-557, 2020, doi.org/10.11821/dlxb202003008.

[47]S. Xie, R. Kuang, and Z. Song, "Variation characteristics of water area of Poyang Lake and its response to meteorological factors," *China Rural Water and Hydropower*, no. 7, pp. 103-109, 2022. (in Chinese)

[48]S. Yao, C. Li, and B. Xue, "Elevation of basal lacustrine sediments along the mid-lower reaches of the Yangtze River and its implications for the reconstruction of Holocene water levels," *Science China Earth Sciences*, vol. 67, no. 9, pp. 2924-2936, 2024, doi: 10.1007/s11430-023-1374-y. (in Chinese)

[49]Z. Dai, L. Xia, and P. Kong et al., "Remote sensing monitoring and analysis of Poyang Lake water area changes over the past 20 years," *Meteorology and Disaster Reduction Research*, vol. 44, no. 2, pp. 127-132, 2021. (in Chinese)

[50]A. Reinart, and M. Reinhold, "Mapping surface temperature in large lakes with MODIS data," *Remote Sensing of Environment*, vol. 112, no. 2, pp. 603-611, 2008, doi: 10.1016/j.rse.2007.05.015B.

[51]Zhu, D. Zhang, and C. Ha et al., "Variation Characteristies of the Ground Temperatures on the Northern Shore of the Qinghai Lake," *Journal of Glaciology and Geocryology*, vol. 32, pp. 844-850, 2010. (in Chinese)

[52]A. J. Prata, "A new long‐wave formula for estimating downward clear‐sky radiation at the surface," *Quarterly Journal of the Royal Meteorological Society*, vol.122, no. 533, pp. 1127-1151, 1996, doi: 10.1002/qj.49712253306.

[53]Z. Li, S. Lyu, and L. Zhao et al., "Turbulent transfer coefficient and roughness length in a high-altitude lake, Tibetan Plateau," *Theoretical and Applied Climatology*, vol. 124, pp. 723-735, 2016, doi: 10.1007/s00704-015-1440-z.

[54]S. Wang, "The research about the facility fishery micro-climate mechanism and theirs influence on aquatic animals," Master's thesis, Anhui Agricultural University, 2005. (in Chinese)

[55]D. Yang, Z. Yao, and Z. Jin et al., "Harmonic analysis of temperature diurnal variation for different types marine aquaculture water," *Chinese Journal of Agrometeorology*, vol. 38, no. 09, pp. 558, 2017, doi: 10.3969/j.issn.1000-6362.2017.09.003.

[56]J. D. McMillen, and W. J. Steenburgh, "Impact of microphysics parameterizations on simulations of the 27 October 2010 Great Salt Lake–effect snowstorm," *Weather and Forecasting*, vol. 30, no. 1, pp. 136-152, 2015, doi: 10.1175/WAF-D-14-00060.1.

[57]J. L. Case, "From drought to flooding in less than a week over South Carolina," *Results in Physics*, vol. 6, pp. 1183-1184, 2016, doi: 10.1016/j.rinp.2016.11.012.

[58]A. Gaur, M. Lacasse, and M. Armstrong et al., "Effects of using different urban parametrization schemes and land-cover datasets on the accuracy of WRF model over the City of Ottawa," *Urban Climate*, vol. 35, 100737, 2021, doi: 10.1016/j.uclim.2020.100737.

[59]R. H. Johns, and C. A. Doswell III, "Severe local storms forecasting," *Weather and Forecasting*, vol. 7, no. 4, pp. 588-612, 1992, doi: 10.1175/1520-0434(1992)007<0588:SLSF>2.0.CO;2.

[60]M. L. Weisman, C. Evans, and L. Bosart, "The 8 May 2009 superderecho: Analysis of a real-time explicit convective forecast," *Weather and Forecasting*, vol. 28, no. 3, pp. 863-892, 2013, doi: 10.1175/WAF-D-12-00023.1.

[61]H. Fujinami, H. Hirata, and M. Kato, et al., "Mesoscale precipitation systems and their role in the rapid development of a monsoon depression over the Bay of Bengal," *Quarterly Journal of the Royal Meteorological Society*, vol. 146, no. 726, pp. 267-283, 2020, doi: 10.1002/qj.3672.

[62]M. W. Moncrieff, and M. J. Miller, "The dynamics and simulation of tropical cumulonimbus and squall lines," *Quarterly Journal of the Royal Meteorological Society*, vol. 102, no. 432, pp. 373-394, 1976, doi: 10.1002/qj.49710243208.

[63]T. M. Weckwerth, and D. B. Parsons, "A review of convection initiation and motivation for IHOP_2002," *Monthly Weather Review*, vol. 134, no. 1, pp. 5-22, 2006, doi: 10.1175/MWR3067.1.

[64]Y. Du, G. Chen, "Heavy rainfall associated with double low-level jets over southern China. Part II: Convection initiation," *Monthly Weather Review*, vol. 147, no. 2, pp. 543-565, 2019, doi: 10.1175/MWR-D-18-0102.1.

[65]S. Piccolroaz, S. Zhu, and R. Ladwig et al., "Lake water temperature modeling in an Era of climate change: Data sources, models, and future prospects," *Reviews of Geophysics*, vol. 62, no. 1, pp. e2023RG000816, 2024, doi: 10.1029/2023RG000816.

Miaoxia Tian received the B.S. degrees from Tianjin Chengjian University, Tianjin, China, in 2022.

She is a graduate student with the Jiangxi Normal University, Jiangxi, China. Her research interests include remote sensing of lakes.

Haibo Zou received the B.S. and M.S. degrees from Sun Yat-sen University, Guangzhou, China, in 2006 and 2009, respectively, and the Ph.D. degree from Lanzhou University, Lanzhou, China, in 2020.

He is a Professor with the Key Laboratory of Poyang Lake Wetland and Watershed Research of Ministry of Education, School of Geography and Environmental Science, Key Laboratory of Natural Disaster Monitoring, Early Warning and Assessment of Jiangxi Province, Jiangxi Normal University, Nanchang, China. His research interests include atmospheric model and Doppler weather radar.

Dr. Zou was a recipient of the National Yong Excellent Workers of Meteorological Science and Technology in 2014, the New Century Excellent Talents in Jiangxi Province of China in 2020.

Jing Zheng received the B.S. degrees from Chengdu University of Information Technology, Sichuan, China, in 2009.

She is the chief forecaster of China Meteorological Administration, one of the top ten forecasters in China, and a full senior engineer. Her research interests include weather and climate forecasting.

Anning Huang received the B.S. degrees from Yunnan University, Yunnan, China, in 2002, joined the School of Atmospheric Sciences of Nanjing University in the same year, received his Ph.D. degree in Meteorology in 2007, and stayed in the university as a professor.

He is a professor at the School of Atmospheric Sciences, Nanjing University. His research interests include land surface process model development and assessment, land-air interactions, and climate modelling and prediction in East Asia.

He was awarded the '14th National Outstanding Young Meteorological Scientist' in 2014, and was selected as one of the outstanding young backbone teachers of Jiangsu universities under the 'Blue and Blue Project' in 2016.

Qi Huang Ph.D. degree from Nanjing Institute of Geography & Limnology, Chinese Academy of Sciences, China, in 2015.

He is the Director of the Field Comprehensive Experimental Station of Nanji Wetland, Poyang Lake, Jiangxi Normal University, and the Head of the Natural Heritage Department of the UNESCO Space Technology Centre for Natural and Cultural Heritage, Nanchang Sub-centre (HIST-NB). His research areas of interest include hydro-ecological surveys, evaluations and long-term positional observations in the middle and lower reaches of the Yangtze River Basin.